TRPV1 structures in nanodiscs reveal mechanisms of ligand and lipid action

Yuan Gao[1,2], **Erhu Cao**[1,*], **David Julius**[1], and **Yifan Cheng**[2,3]

[1]Department of Physiology, University of California, San Francisco, California 94143, USA

[2]Keck Advanced Microscopy Laboratory and Department of Biochemistry and Biophysics, University of California, San Francisco, California 94143, USA

[3]Howard Hughes Medical Institute, University of California, San Francisco, California 94143, USA

Abstract

When integral membrane proteins are visualized in detergents or other artificial systems, an important layer of information is lost regarding lipid interactions and their effects on protein structure. This is especially relevant to proteins for which lipids play both structural and regulatory roles. Here, we demonstrate the power of combining electron cryo-microscopy with lipid nanodisc technology to ascertain the structure of the TRPV1 ion channel in a native bilayer environment. Using this approach, we determined the locations of annular and regulatory lipids and showed that specific phospholipid interactions enhance binding of a spider toxin to TRPV1 through formation of a tripartite complex. Furthermore, phosphatidylinositol lipids occupy the binding site for capsaicin and other vanilloid ligands, suggesting a mechanism whereby chemical or thermal stimuli elicit channel activation by promoting release of bioactive lipids from a critical allosteric regulatory site.

Transporters and ion channels reside in biological membranes, where lipids play important structural and regulatory roles[1–3]. However, structural characterization of protein-lipid interactions is challenging in detergent-based systems, making implementation of more

native, lipid-based environments an important goal. For crystallographic approaches, this has been achieved through the use of lipidic-cubic phase systems[4,5] or formation of two-dimensional crystals in lipid bilayers[6]. For single particle electron microscopy, one approach is to reconstitute proteins into spherical liposomes for random-spherically constrained single particle reconstruction[7]. Another is to use lipid nanodiscs, hockey puck-like structures in which a lipid bilayer patch is encircled by an amphipathic scaffolding protein[8]. Both approaches mimic the native lipid environment and can enhance functionality and thermal stability[9,10]. Moreover, nanodisc-embedded proteins are often monodisperse and especially suitable for single particle electron cryo-microscopy (cryo-EM)[11,12]. Nevertheless, membrane protein structures determined with these systems have achieved limited resolution to-date, failing to reveal detailed protein-lipid interactions.

Cryo-EM can now be used to obtain structures of many biological macromolecules at near atomic resolution[13–15]. An important next goal is to enable cryo-EM to define interactions between small molecules and their protein targets at the atomic level. The heat- and capsaicin-activated ion channel, TRPV1, is an excellent model with which to address these challenges. This sensory receptor is modulated by membrane lipids and their metabolites, and activated or inhibited by various ligands, including vanilloid compounds and peptide toxins[16,17]. Moreover, TRPV1 structures in multiple conformational states have recently been determined by cryo-EM under conditions in which purified channel protein was stabilized with an amphipathic polymer[18,19]. These structures provide a standard against which other preparations can be assessed. Here we show that high-resolution structures can be obtained when TRPV1 is embedded in a nanodisc and use this system to characterize channel-lipid interactions, revealing novel structural mechanisms underlying ligand binding and channel gating.

Structure of TRPV1 in lipid nanodiscs

We reconstituted purified TRPV1 protein into lipid nanodiscs generated with different membrane scaffold proteins (MSPs) (Extended Data Fig. 1). For structural analysis, we favored preparations using MSP2N2, which forms nanodiscs of ~150Å diameter and is sufficient to accommodate TRPV1 without imposing spatial constraint (Extended Data Fig. 1d). Indeed, cryo-EM images of frozen hydrated samples revealed monodispersed TRPV1-nanodisc particles. 2D class averages showed TRPV1 tetramers with distinct channel features floating within the nanodisc (top view) (Fig. 1a). Transmembrane helices and cytoplasmic domains were clearly visible within a disc-like density contributed by the lipid bilayer (side views). Importantly, the presence of the bilayer and MSP did not preclude accurate image alignment.

We determined three structures of TRPV1 in nanodiscs, including unliganded, agonist-bound, and antagonist-bound states at resolutions of 3.2, 2.9, and 3.4Å, respectively (Fig. 1b; Extended Data Figs. 2–4). These structures can be compared directly to those previously obtained in amphipol[18,19]. Generally speaking, density maps determined with nanodiscs were of superior quality. This is especially evident when examining side chain densities within transmembrane regions or connecting loops that face lipids, such as S1 and S2 helices and the S2–S3 linker (Extended Data Fig. 5a–f). Interestingly, improvements were not

limited to transmembrane regions, but also extended to cytoplasmic domains, enabling us to build a model including previously unresolved regions (Extended Data Fig. 6a, b). These improved density features may reflect enhanced stability of the channel in the nanodisc, but other technical advances also contribute (Extended Data Table 1). The nanodisc- and amphipol-stabilized structures of a given conformational state are essentially identical, albeit with some specific differences that may relate to lipid and/or ligand binding (see below).

Two layers of continuous density corresponding to lipid head groups mark the bilayer boundaries and surround the channel (Fig. 1a, b and Extended Data Fig. 7a). Furthermore, well-resolved lipid-like densities associate with various regions of the channel, indicative of well-ordered lipids that form specific protein interactions (Fig. 1b and Extended Data Fig. 7b, c). These include annular lipids that fill crevices between subunits and reside within the outer leaflet surrounding pore-forming domains of the channel, reminiscent of voltage gated potassium channels[20]. We also observed lipids in hydrophobic clefts, as exemplified by a density within the lower segment of the S1–S4 domain, whose shape and local environment suggest that it represents a molecule of phosphatidylcholine (Extended Data Fig. 7c). Indeed, we observed a similar density in this location for TRPV1 in amphipol[19], suggesting that an endogenous, tightly bound lipid helps stabilize a hydrophobic crevice within the S1–S4 domain, which remains stationary during channel gating[18].

Lipid-channel-toxin tripartite complex

TRPV1 can be stably trapped in its fully open state when exposed to resiniferatoxin (RTX) - an ultra-potent vanilloid agonist[18,21] - plus double-knot toxin (DkTx), a bivalent tarantula peptide that consists of two nearly identical inhibitor cysteine knot (ICK) motifs joined by a short (7 amino acid) linker[22]. Two DkTx molecules bind to one TRPV1 tetramer such that each knot assumes a specific orientation with respect to the channel, suggesting that two DkTx molecules adopt an anti-parallel configuration[18]. In our current nanodisc structure, we initially applied C4 symmetry to achieve optimal resolution, yielding a 2.9Å map of the nanodisc-stabilized, RTX/DkTx-activated channel, compared to 3.8Å for the amphipol-stabilized complex (Fig. 2a and Extended Data Fig. 8). To gain further information about non-equivalent regions of the toxin, we applied C2 symmetry independently, which was insufficient to reveal specific features associated with each knot and their relationship to one another, indicating that some particle images were misaligned by 90° around the symmetry axis. Focused classification on the toxin and adjacent regions enabled us to partially separate the two possible orientations to obtain an improved C2 averaged map, as evidenced by more pronounced features within the antiparallel linker connecting the ICK knots (Fig. 2b and Extended Data Fig. 8).

With improved maps, we rebuilt and refined the atomic model of the fully open channel with associated ligands. For DkTx, three canonical disulfide bonds are clearly resolved, as are most side chains in regions that interact with TRPV1 (Fig. 2a and Extended Data Fig. 8b). Here we find that residues involved in channel interaction are highly conserved between ICK knots, consistent with the fact that side chain densities of these residues were well resolved even when C4 symmetry was applied. Interestingly, the density of the linker domain is also

well resolved (Fig. 2c), revealing a taut and constrained conformation that likely contributes to high avidity interaction with the channel[22].

The nanodisc system enabled us to determine where interactions occur with respect to the lipid bilayer. Two hydrophobic fingers from each ICK knot insert into the bilayer (Fig. 2a) and several phospholipid densities at these sites are well resolved, likely reflecting their stabilization through specific toxin interactions (Fig. 2c, d and Extended Data Fig. 7b). For example, a tryptophan side chain in finger 1 (Trp11 of knot 1 and Trp53 of knot 2) interacts with the aliphatic tail of a phospholipid whose head group forms a polar interaction with Arg534 in TRPV1, located in the extracellular loop connecting S3 and S4 helices. This sort of tripartite complex between toxin, lipid, and channel is also seen proximal to finger 2, where a phenylalanine side chain (Phe27 of knot 1 and Phe67 of knot 2) is stabilized through hydrophobic interaction with an aliphatic lipid tail. Furthermore, the lipid head group is coordinated by the side chain of Ser629 at the top of the channel's pore helix domain, as well as by interaction with Tyr453 from S1 of the adjacent channel subunit (Fig. 2d). Thus, together with the newly refined apo model, we see that gating-associated side chain movements within outer pore loops and pore helices are more clearly visualized compared with our previous structures in amphipols (Extended Data Fig. 5b). These new observations demonstrate how potential side chain clashes between DkTx and the apo channel are relieved through lateral shifts in the outer pore loops and pore helices, primarily through reorientation of aromatic side chains (Fig. 3a). Moreover, they suggest a structural mechanism for how toxin binding stabilizes the open state.

The nanodisc preparation also reveals local distortions in the lipid environment associated with toxin binding. For example, insertion of DkTx into the bilayer results in lateral and upward displacement of a phospholipid adjacent to finger 1, as well as lateral and downward displacement of another phospholipid proximal to finger 2 (Fig. 3b). The resulting energetic penalty may be compensated by toxin-channel interactions, as well as by new interactions formed between the channel and displaced lipids (Figs. 2d and 3b). Such a tripartite arrangement likely determines the overall affinity and kinetics of toxin binding.

A resident lipid in the vanilloid pocket

A particularly striking density within the vanilloid binding pocket of the apo channel can be confidently interpreted as a phosphatidylinositol lipid whose branched acyl chains extend upward between S4 of one subunit and S5 and S6 of an adjacent subunit, within a hydrophobic cleft facing the lipid bilayer. The inositol ring is bounded on each side by S3 and the elbow of the S4–S5 linker, with the TRP domain below (Fig. 4a). Polar interactions, such as that between Arg557 at the bottom of S4 and the hydroxyl group of the phosphate on position 1, or between Glu570 in the S4–S5 linker and a hydroxyl group on position 6 of the inositol ring, further enhance stability (Fig. 4a and Extended Data Fig. 9a). Detailed analysis of the local protein environment suggests that additional phosphate groups at positions 3, 4 and/or 5 of the inositol ring could form electrostatic interactions with Arg409 in a cytoplasmic N-terminal segment preceding S1 or Lys571 and Arg575 within the S4–S5 linker (Fig. 4a and Extended Data Fig. 9a, b). If so, then this pocket could favor a range of phosphatidylinositide species.

A similar, albeit less well resolved density was observed at this locale in our amphipol-stabilized structure[19], suggesting that a tightly associated lipid is retained during channel purification. This, or other associated lipids may derive from the soybean lipid extract that was added to improve protein stability, but it is also possible that they are of cellular origin.

Mechanism of vanilloid action

We next examined the structure of the vanilloid pocket when occupied by various ligands (Extended Data Fig. 9c, d). With nanodiscs, we could discern ligand structures in much greater detail compared to amphipol-stabilized structures. For example, RTX could be precisely fit by its atomic structure (Fig. 4b), and in a manner consistent with mutagenesis and modeling studies[23–28]. For the capsaicin-like homovanillyl ester moiety, key interactions include a hydrogen bond between Thr550 and the carbonyl oxygen proximal to the vanilloid moiety, as well as between Ser512 and Arg557 and the vanilloid moiety at the hydroxyl group. Tyr511, which assumes distinct rotamers in apo versus liganded TRPV1 structures[18], engages in hydrogen bonding with the ester oxygen of RTX. The five-membered diterpene ring component of RTX is stabilized by hydrophobic interactions with several amino acids, including Leu515, Val518, Met547, and Ile573, as well as Leu669 from a neighboring subunit. These residues form a hydrophobic pocket that accommodates the heterocyclic region of the drug, likely accounting for high affinity binding of this potent agonist.

Comparison of apo versus RTX-bound states suggests that vanilloid agonists function by displacing the resident phosphatidylinositol lipid. Indeed, RTX docks within the same pocket otherwise occupied by one acyl chain of the lipid. Absence of the other acyl chain allows for reorientation of Tyr511 to further stabilize RTX binding (Extended Data Fig. 9c, d). At the same time, RTX binding coordinates interaction between Arg557 and Glu570 to re-occupy the space vacated by the inositol head group, consequently pulling the S4–S5 linker away from the central axis to facilitate opening of the lower gate (Fig. 5 and Extended Data Fig. 9e). This mechanism is further supported by analysis of a capsazepine-bound structure (determined in either amphipol or nanodisc), in which this competitive vanilloid antagonist[29] occupies the same hydrophobic pocket as RTX, but apparently without facilitating the key interaction between Arg557 and Glu570 (Fig. 5 and Extended Data Fig. 9f). Indeed, mutations at these sites abrogate capsaicin-evoked responses, whereas charge-swapping mutations (R557E and E570R) partially restore channel function[28,30], consistent with our model. Parenthetically, we did not observe significant movement within the S1–S4 region (Extended Data Fig. 9e), indicating that the static nature of this voltage sensor-like domain as previously described[18] is not merely an artifact of amphipol packing.

Concluding remarks

Membrane proteins have been reconstituted into lipid nanodiscs and studied by single particle cryo-EM[11,12], but our results now show that this system can be taken to atomic resolution, enabling detailed structural analysis of lipid-protein interactions in a more native or stable environment. A main concern about using nanodiscs for cryo-EM was that the bilayer mass would weaken the power of image alignment and limit achievable resolution of imbedded proteins. Our results now show that this is not a problem. Indeed, as in the case of

amphipol-stabilized TRPV1, the transmembrane core reached highest resolution, indicating that image alignment was not adversely affected by the nanodisc. In addition to enabling visualization of specific, tightly bound lipids, the nanodisc provides a defined contour for the bilayer in relation to protein structure while revealing local deformations such as those associated with toxin binding.

Biophysical and biochemical studies suggest that amphipathic ICK toxins, such as hanatoxin and SGTx1, first partition into the lipid bilayer, then engage their channel target through moderate affinity protein-protein interactions[31]. Furthermore, binding affinity may be enhanced by formation of a toxin-lipid-channel trimolecular complex[32,33]. Our DkTx-bound TRPV1 structure supports this concept by showing that hydrophobic fingers of the toxin insert almost halfway (~9Å) through the outer leaflet of the bilayer, interaction surfaces between DkTx and TRPV1 are not extensive, and membrane lipids form bridging interactions between toxin and channel (Fig. 6a). Indeed, we achieved significantly better resolution for the RTX/DkTx-bound channel, likely reflecting enhanced stability of such a tripartite complex. Overall, our findings are consistent with recent modeling studies based on a nuclear magnetic resonance structure of DkTx[34]. Lastly, DkTx is uniquely bivalent, and our structure suggests that the taut linker region connecting the two ICK knots has evolved to perfectly match the distance between subunit binding sites, which, together with the specific anti-parallel orientation of toxin binding, likely contributes to the remarkable avidity and specificity of the DkTx-TRPV1 interaction.

Many TRP channels function as 'receptor-operated' channels that are modulated by phospholipase C-mediated phosphatidylinositol-4,5-bisphosphate (PIP_2) hydrolysis[35,36]. However, structural mechanisms governing phosphatidylinositide-mediated regulation remain poorly understood. For TRPV1, it is not clear whether PIP_2 or other phosphatidylinositides bind directly to the channel, or function as obligatory co-factors, allosteric inhibitors, or both[2,37]. Moreover, channel domains that specify phosphatidylinositide sensitivity have not been unambiguously identified. We now show that phosphatidylinositides function as endogenous, tightly bound co-factors that stabilize TRPV1 in its resting state by serving as competitive vanilloid antagonists and negative allosteric modulators. At the same time, phosphatidylinositides may function as positive, obligatory co-factors whose binding to TRPV1 in the closed state primes the channel for subsequent activation by vanilloids or other stimuli (Fig. 6b). Thus, our structures suggest a dual role for phosphatidylinositides through interactions at this single site. Moreover, structure-function studies suggest that regions within the TRPV1 C-terminus interact with PIP_2 (ref [38–41]) and thus additional mechanisms may contribute to phosphatidylinositide regulation of TRPV1 or other TRP subtypes. Our findings, together with those describing PIP_2 interactions with inwardly rectifying potassium channels[42], demonstrate that phosphatidylinositides can interact with membrane proteins in diverse ways. It is tempting to speculate that temperature-dependent displacement of endogenous phosphatidylinositides contributes to heat-evoked activation of TRPV1 (Fig. 6c).

METHODS

Protein expression, purification and nanodisc reconstitution

A minimal functional rat TRPV1 construct was expressed and purified as previously described [19]. Membrane scaffold proteins MSP2N2 and MSP1E3 were expressed and purified from *E. coli*, and detergent solubilized TRPV1 protein incorporated into lipid nanodisc as previously described[10], with modifications. Briefly, 2.5 mg soybean polar lipid extract (Avanti) dissolved in chloroform was dried using argon stream and residual chloroform further removed by vacuum desiccation (~ 3hrs). Lipids were then rehydrated in buffer (20 mM HEPES, 150mM NaCl, 2mM TCEP, 14 mM DDM, pH 7.4) and sonicated, resulting in a clear lipid stock at 10mM concentration. Purified MBP-TRPV1 protein (0.7– 1.5 mg ml^{-1}) solubilized in 0.5 mM DDM was mixed with the soybean lipid stock and MSP2N2 (~3mg ml^{-1}) at various molar ratios and incubated on ice for 30 minutes. Specifically, we achieved the best result using the ratio (TRPV1 monomer : MSP : soybean lipid = 1:1:150 – 1:1.5:225) for MSP2N2 and 1:1:100 for MSP1E3. Bio-beads SM2 (20 mg per 1ml mixture, Bio-rad) were added to initiate the reconstitution by removing detergents from the system and the mixture incubated at 4°C for one hour with constant rotation. A second batch of Bio-beads (equal amount) together with TEV protease (40 µg per 1mg TRPV1) was then added and the sample incubated at 4°C overnight. Bio-beads were then removed and the reconstitution mixture cleared by centrifugation before subsequent separation on a Superose 6 column (GE) in buffer (20 mM HEPES, 150mM NaCl, 2mM TCEP, pH 7.4). Reconstitution was assessed by size exclusion chromatography, SDS-PAGE, and negative stain EM (Extended Data Fig. 1). The peak corresponding to tetrameric TRPV1 reconstituted in lipid nanodisc was collected for analysis by both negative stain and cryo-EM. TRPV1-nanodisc particles were mono-dispersed as assessed by negative stain EM (Extended Data Fig. 1c).

EM data acquisition and analysis

Grids of TRPV1-nanodisc complexes for negative-stain EM were prepared following an established protocol[43]. Specifically, 2.5 µl of purified TRPV1-nanodisc complex (0.05 – 0.1mg ml^{-1}) was applied to glow-discharged EM grids covered by a thin layer of continuous carbon film and stained with 0.75% (w/v) uranyl formate. Negatively stained EM grids were imaged on a Tecnai T12 microscope (FEI Company) with a thermoionic electron source (LaB$_6$) and operated at 120 kV. Images were recorded at a nominal magnification of 52,000X and a defocus set to −1.5 µm using a 4k×4k scintillator based charge-coupled device camera (UltraScan 4000, Gatan), corresponding to a pixel size of 2.02Å on the specimen.

For cryo-EM, 2.5 µl of purified TRPV1-nanodisc complex (~0.5 mg ml^{-1} concentration and supplied with 2.5% (v/v) glycerol) was applied to a glow-discharged Quantifoil grid (holey carbon film with 1.2µm hole size and 1.3 µm hole spacing on 400 mesh Cu grid), blotted with a Vitrobot Mark III (FEI Company) using 8-s blotting time with 100% humidity at 5°C, and plunge frozen in liquid ethane cooled by liquid nitrogen. For preparation of TRPV1-nanodisc in complex with agonists or antagonist, reconstituted channel complex was mixed with RTX (final concentration 50 µM; molecular weight 628 Da) and DkTx (final

concentration 20 μM; molecular weight 8.5 kDa), or capsazepine (20 μM; molecular weight 377 Da), 20 minutes before vitrification, as described above.

Cryo-EM images of frozen hydrated TRPV1-nanodisc particles were collected on a TF30 Polara electron microscope (FEI Company) equipped with a field emission electron source and operated at 300 kV. Images were recorded at a nominal magnification of 31,000 X using a K2 Summit direct electron detector camera (Gatan) operated in super-resolution counting mode following an established protocol [44]. Images have a calibrated physical pixel size of 1.22 Å per pixel on the specimen. The dose rate on the camera was set to be 8.2 counts (corresponding to 9.9 electrons) per physical pixel per second. The total exposure time was 6 s, leading to a total accumulated dose of 41 electrons per Å^2 on the specimen. Each image was fractionated into 30 subframes, each with an accumulation exposure time of 0.2 s. All dose-fractionated cryo-EM images were recorded using a semi-automated acquisition program UCSFImage4 (ref [45]). Images were recorded with a defocus in a range from −0.7 to −2.2 μm.

Image processing

Defocus of all images was determined using CTFFIND4 (ref [46]). Negative stain EM images were 2×2 binned for particle picking and subsequent image processing. SamViewer, an interactive image analysis program written in Python, was used for all 2D image display and manual particle picking. Individual particles were manually picked, boxed out from micrograph and normalized to have a mean of 0 and a standard deviation of 1. Usually a total of 1000 – 2000 particles were picked manually. For 2D classification, particles were first corrected for contrast transfer function (CTF) by flipping the phase using 'ctfapply' (written by X. Li), and then subjected to ten cycles of correspondence analysis, k-means classification and multi-reference alignment, using SPIDER operations 'CA S', 'CL KM' and 'AP SH' (ref [47]). 2D class averages generated from manually picked particles then served as references for a subsequent automatic particle picking procedure implemented in a Python script 'samautopick.py', as previously described[19]. All picked particles were then screened visually and particles without clear, defined structural features were removed interactively. The selected particles were again subjected to the same 2D analysis and 2D class averages were assessed (Extended data figure 1).

For cryo-EM images, dose fractionated super-resolution image stacks of frozen, hydrated TRPV1-nanodisc images were first binned 2×2 by Fourier cropping, resulting in a pixel size of 1.22 Å, for motion correction and further image processing. Each image stack was subjected to whole-frame motion correction [44], followed by correction at individual pixel level using program UcsfDfCorr (written by Shawn Zheng). A sum of all corrected subframes, calculated following a dose weighting scheme [48], was used for further processing. Particle picking was performed similarly as described above. Selected particles after visual screening were boxed out, and subjected directly to maximal likelihood-based 3D classification procedures implemented in RELION [49]. A previous density map of TRPV1 solubilized in amphipol (EMDB code 5778) was low-pass filtered to a resolution of 60 Å and used as initial reference for 3D classification. Stable classes from 3D classification were then iteratively refined and reclassified to obtain the most homogeneous subset for the

final 3D reconstruction. All refinements followed the gold-standard refinement procedure, in which the data set was divided into two half sets, and refined independently. Once refinement was converged, the final data set was subjected to the 'postprocessing' procedure of RELION in which a soft mask was calculated and applied to the two half-maps before the corrected Fourier shell coefficient (FSC) was calculated. B-factor estimation and map sharpening were also performed in this step using an automated procedure. C4-symmetry was applied in all 3D classification and refinement steps unless specifically noted. The final resolution was estimated using the FSC = 0.143 criterion [50] on corrected FSC curves in which the influences of the mask were removed. Local resolution was estimated from unbinned and unsharpened raw density maps using ResMap [51]. Number of particles in each dataset and other details related to data processing are summarized in Extended Data Table 1. Conformations of TRPV1 alone or with ligands are very similar whether determined in amphipol or nanodisc.

For TRPV1-RTX/DkTx nanodisc dataset, two 3D reconstructions were first determined independently to resolutions of 2.95 Å with C4 symmetry and 3.24 Å with C2 symmetry. These two reconstructions are very similar. We then performed a 3D classification focusing on DkTx and its peripheral region in TRPV1, following a procedure outlined in Extended Data Fig 8a. Specifically, a volume that includes DkTx and peripheral densities in TRPV1 was masked out from the C2-symmetrized 3D reconstruction. The density after masking was back-projected and convoluted with the CTF to yield a 2D image for all individual particles using its assigned Euler angles and defocus parameters from the reconstruction. These images were firstly scaled and normalized to the corresponding experimental particle images and then subtracted from the experimental particle images, resulting a particle stack in which every particle image contains only signals for the focused region. These procedures were implemented into a Python script 'projection_subtraction.py' (written by E. Palovcak) using the filt_ctf and math.sub.optimal functions from the SPARX and EMAN2 libraries, respectively [52,53] The modified particle images were then subjected to 3D classification in RELION with a soft mask around DkTx, and without further alignment. Two major classes representing two possible orientations of DkTx (as judged by the linker region) were identified and unsubtracted particles belong to each class were separated and used for two independent reconstructions with pre-determined Euler angles. These two reconstructions were aligned to each other using 'fit in map' in UCSF Chimera [54] and summed yielding a density map with enhanced two-fold symmetry feature. This density map was used as the reference model for a second round of focused 3D classification to further optimize classification result.

We also determined the structure of capsasepine-bound TRPV1 in amphipol A8-35 (Anatrace). In brief, TRPV1 (~ 0.5 mg/ml) in amphipol was mixed with capsazepine (final concentration 50 μM) at 4 °C for ~ 30 minutes prior to application to grids. Procedures for grid preparation, data acquisition and image processing were the same as described [19]. The final resolution of the reconstruction (3.8 Å) was calculated using the 'post-processing' procedure of RELION in which a soft mask was calculated and applied to the two half-maps using default parameters.

Model building

Atomic models of TRPV1 in apo (Protein Data Bank, (PDB) code 3J5P) or fully open states (PDB code 3J5Q), previously determined when the channel was solubilized in amphipol, were initially docked into maps of unliganded or agonist bound TRPV1-nanodisc complex using UCSF Chimera. With improved resolution and stability afforded by the nanodisc system, we were able to remodel side-chains and local geometry to higher accuracy. TRPV1 models were first adjusted and real-space refined using COOT [55]. Unliganded TRPV1 model was then used for modeling capsazepine-bound structure with minor adjustment due to high similarity between the two structures. DkTx was remodeled according to the improved map from focused analysis (see above). All models for ligands or associated lipids, except for RTX, were generated using elBOW [56] module in PHENIX [57] together with their geometric constraints. RTX model and constraints were generated using a web server 'PRODRG' [58]. For simplicity, all annular lipids in the structure were modeled as phosphatidylethanolamine (PE), and the acyl chains of all lipids were modeled as 1 – 8 carbon length according to specific densities. Models for all ligands were docked into densities and refined using COOT. Full models of TRPV1 (residue 335–751, corresponding to well-resolved regions in maps) in complex with ligands and lipids were then subjected to global refinement and minimization in real space using the module 'phenix.real_space_refine' [59] in PHENIX. For cross validation[60], the refined structures were first randomly displaced by 0.1Å and then refined against one of the half maps generated in RELION following the same procedures described above. FSC curves were calculated between the refined model and half map 1 ('work', used in test refinement), the refined model and half map 2 ('free', not used in test refinement), and the refined model and summed map. The small gap between the work and the free FSC curves indicated little effect of over-fitting of atomic models. The geometries of all models were assessed using 'comprehensive model validation' section in PHENIX and MolProbity [61], and detailed information was listed in Extended Data Table 1.

Figures were prepared using UCSF Chimera and 2D EM images were extracted using SamViewer.

Extended Data
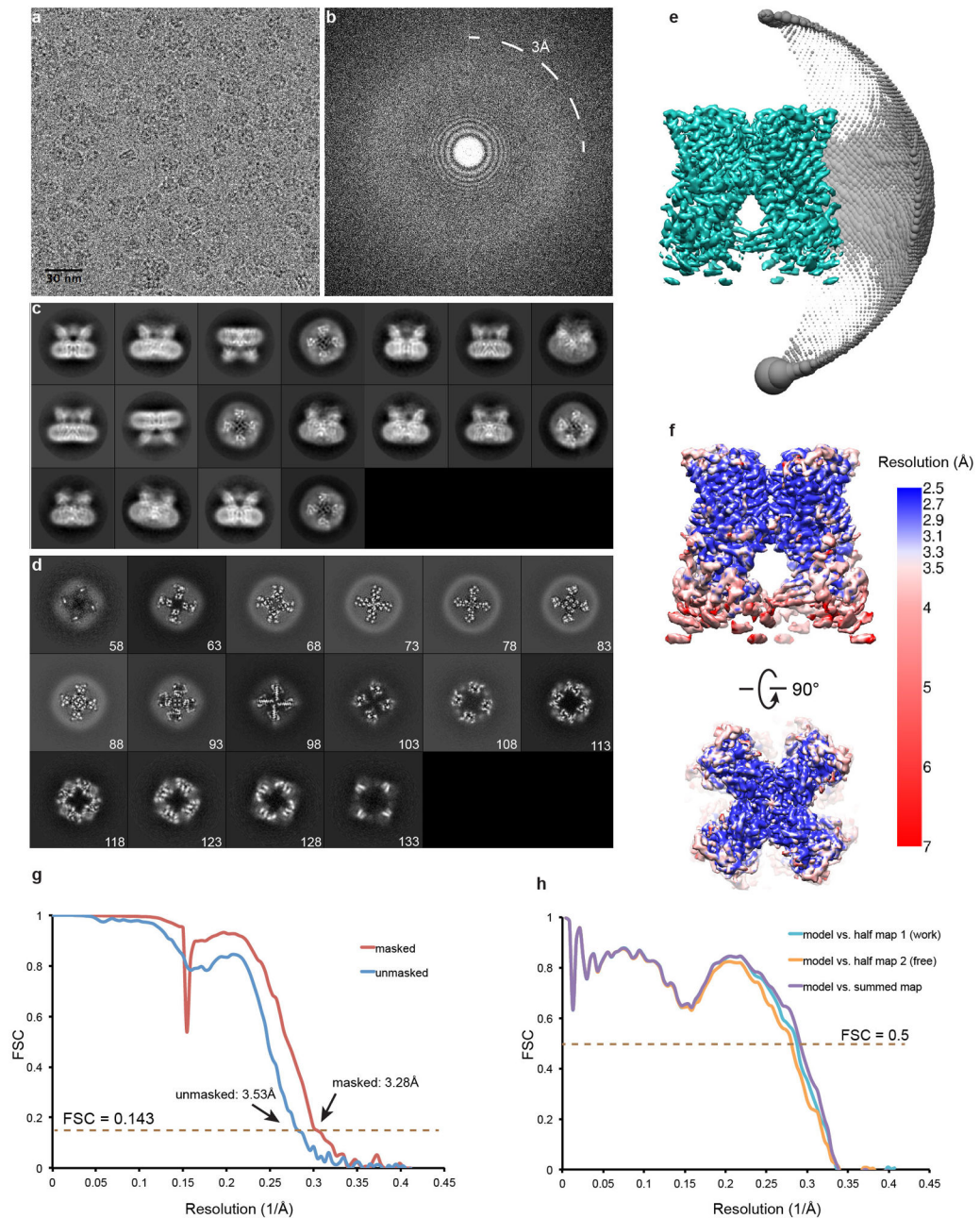
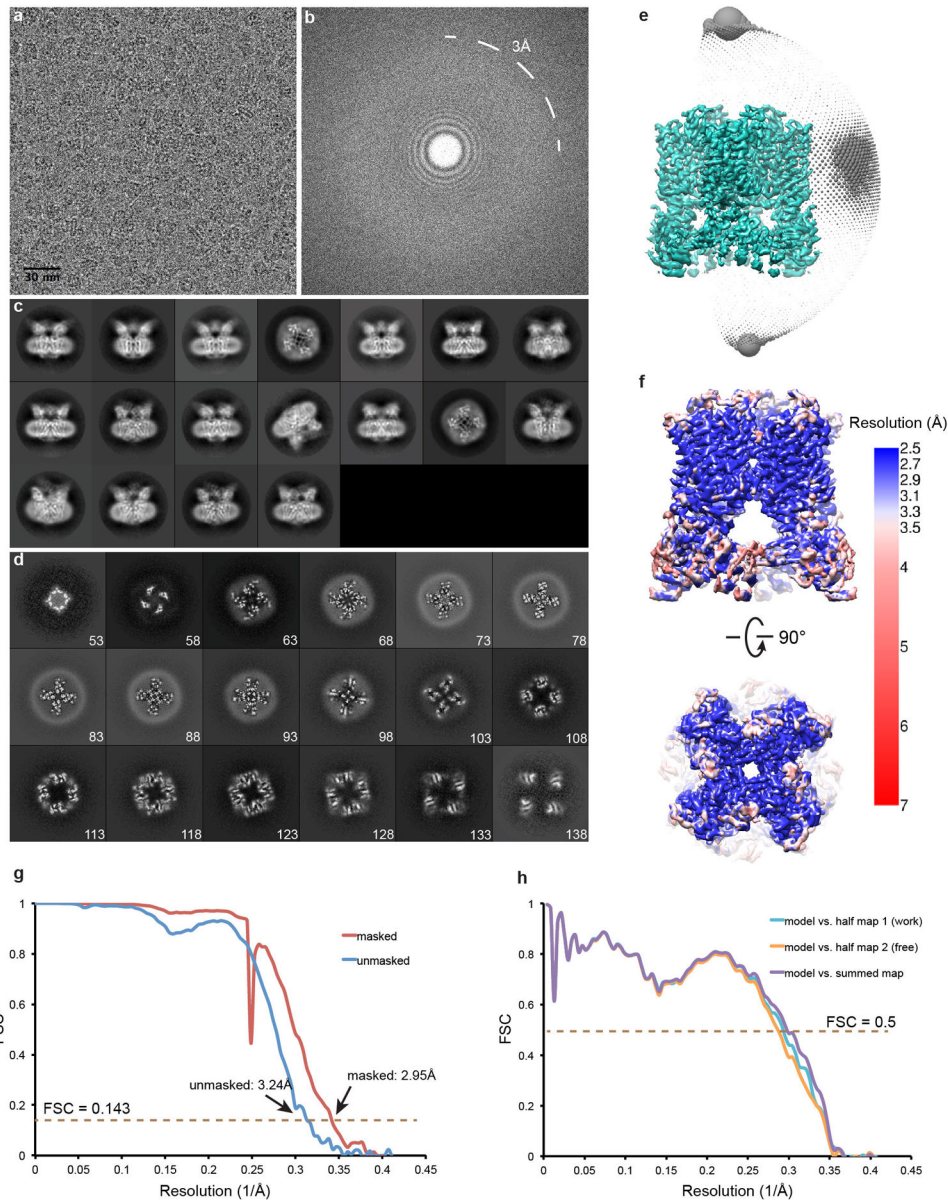**Extended Data Figure 1. Reconstitution of TRPV1 into lipid nanodisc**
a, Size exclusion chromatography of TRPV1 channel reconstituted into lipid nanodisc using MSP2N2. Void volume and peaks corresponding to TRPV1 and cleaved MBP are indicated. **b**, SDS-PAGE of detergent solubilized MBP-TRPV1 fusion protein and material from nanodisc reconstituted with TRPV1 following MBP cleavage (middle peak in **a**). Note the presence of both bands for TRPV1 and MSP2N2. **c**, Representative micrograph of negative-stained TRPV1-nanodisc sample showing mono-dispersed and homogeneous particles. **d**, Reference-free 2D class averages of particles in (c) revealing band-like density contributed

by the lipid disc (side view) and tetrameric arrangement of channel subunits (top view). **e**, 2D class averages of the same protein reconstituted into MSP1E3 nanodisc, which is smaller in diameter. Note the extra space within the disc offered by MSP2N2 scaffold protein in (d).
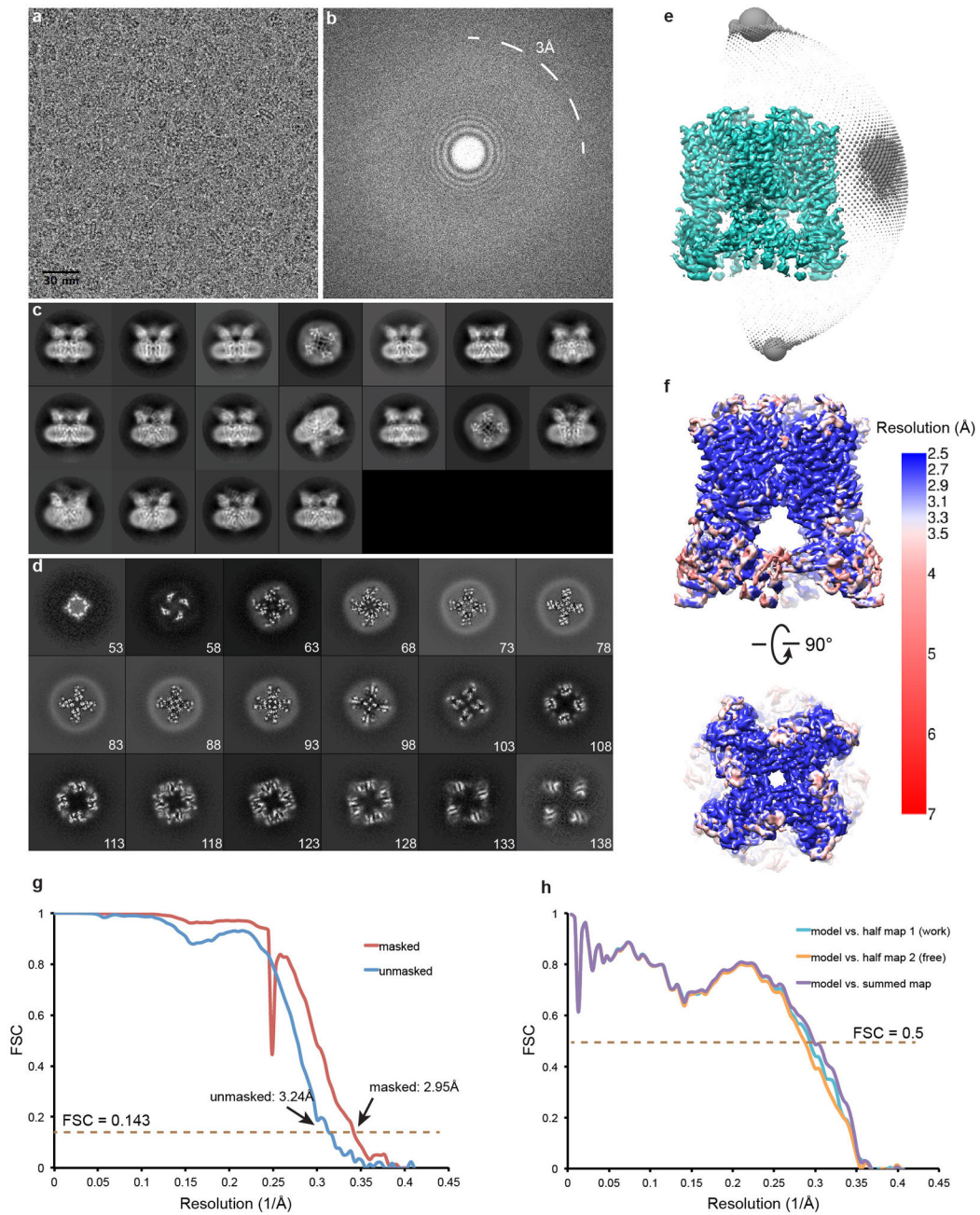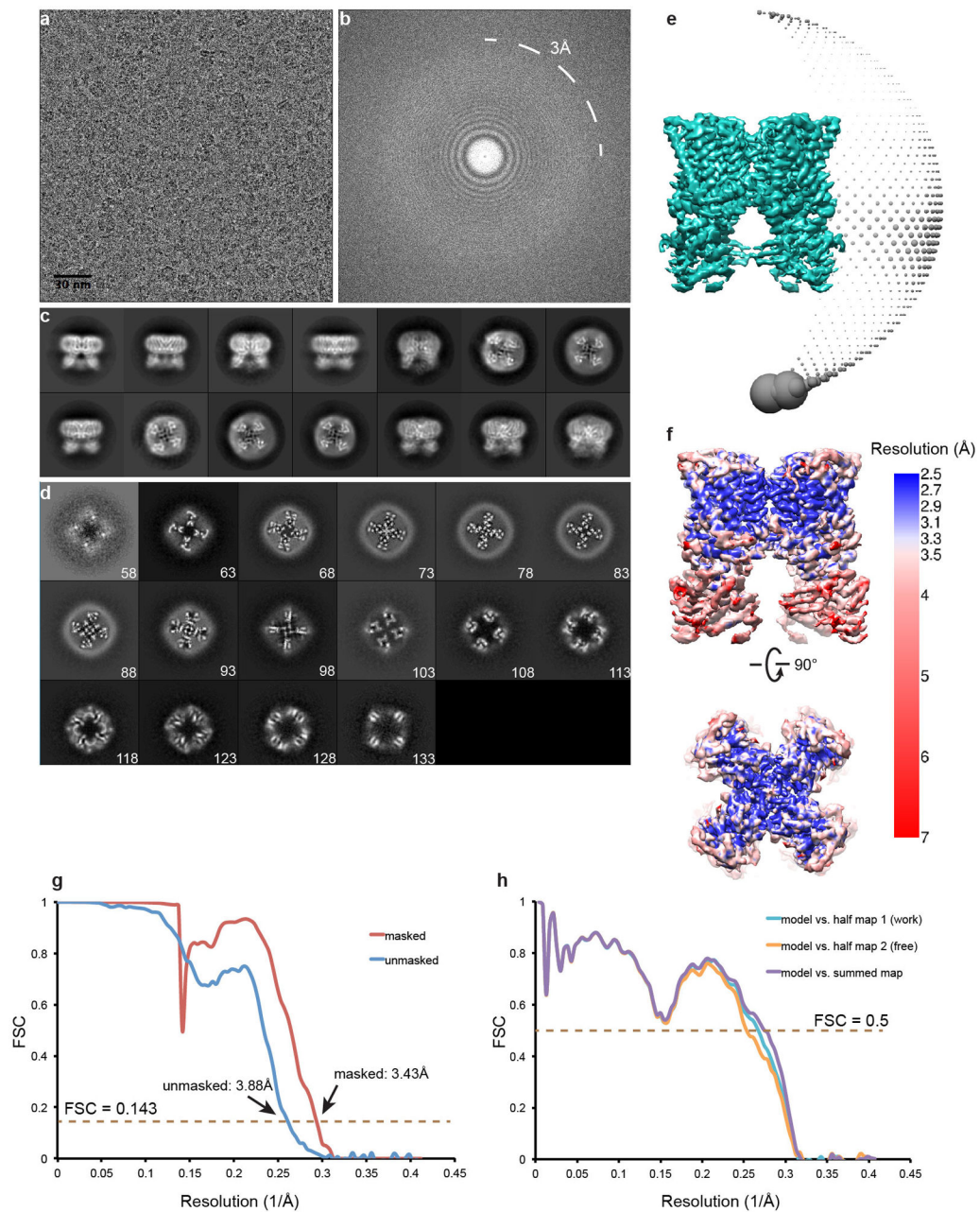

Extended Data Figure 2. Single-particle cryo-EM of unliganded TRPV1 in lipid nanodisc
a, Representative raw micrograph of apo TRPV1 in nanodisc. **b**, Fourier transform of image in (**a**). Note Thon rings are visible to up to 3Å. **c**, Gallery of 2D class averages. **d**, Slices through the unsharpened density map at different levels along the channel symmetry axis (numbers start from extracellular side). **e**, Euler angle distribution of all particles included in

the calculation of the final 3D reconstruction. Position of each sphere (grey) relative to the density map (green) represents its angle assignment and the radius of the sphere is proportional to the amount of particles in this specific orientation. **f**, Final 3D density map colored with local resolution in side and top views. **g**, FSC curves between two independently refined half maps before (blue) and after (red) the post-processing in RELION. **h**, FSC curves for cross validation: model versus summed map (purple), model versus half map 1 (used in test refinement, cyan), model versus half map 2 (not used in test refinement, orange). Small differences between the "work" and the "free" curves indicate little effect of over-fitting.

Extended Data Figure 3. Single-particle cryo-EM studies of agonist-bound TRPV1 in lipid nanodisc
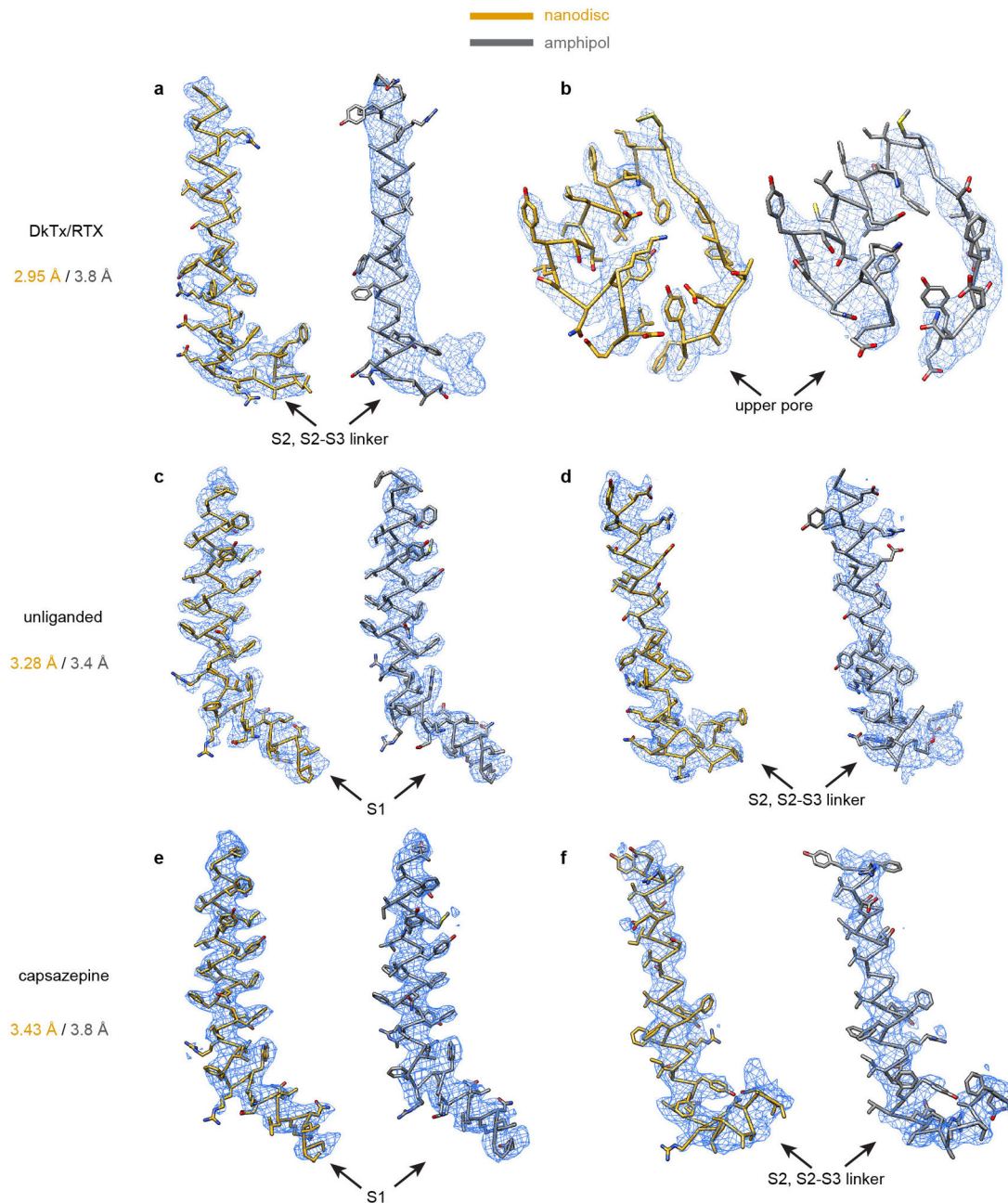
a, Representative raw micrograph of TRPV1-RTX/DkTx in nanodisc. **b**, Fourier transform of image in (**a**). **c**, Gallery of 2D class averages. **d**, Slices through the unsharpened density map at different levels along the channel symmetry axis (numbers start from extracellular side). **e**, Euler angle distribution of all particles included in the calculation of the final 3D reconstruction. Position of each sphere (grey) relative to the density map (green) represents its angle assignment and the radius of the sphere is proportional to the amount of particles in this specific orientation. **f**, Final 3D density map colored with local resolution in side and top views. **g**, FSC curves between two independently refined half maps before (blue) and after (red) the post-processing in RELION. **h**, FSC curves for cross validation: model versus summed map (purple), model versus half map 1 (used in test refinement, cyan), model versus half map 2 (not used in test refinement, orange). Small differences between the "work" and the "free" curves indicate little effect of over-fitting.

Extended Data Figure 4. Single-particle cryo-EM studies of antagonist-bound TRPV1 in lipid nanodisc

a, Representative raw micrograph of TRPV1/capsazepine complex in nanodisc. **b**, Fourier transform of image in (**a**). **c**, Gallery of 2D class averages. **d**, Slices through the unsharpened density map at different levels along the channel symmetry axis (numbers start from extracellular side). **e**, Euler angle distribution of all particles included in the calculation of the final 3D reconstruction. Position of each sphere (grey) relative to the density map (green) represents its angle assignment and the radius of the sphere is proportional to the amount of particles in this specific orientation. **f**, Final 3D density map colored with local resolution in side and top views. **g**, FSC curves between two independently refined half maps before

(blue) and after (red) the post-processing in RELION. **h**, FSC curves for cross validation: model versus summed map (purple), model versus half map 1 (used in test refinement, cyan), model versus half map 2 (not used in test refinement, orange). Small differences between the "work" and the "free" curves indicate little effect of over-fitting.

Extended Data Figure 5. Improved resolution for structures determined in nanodisc
Comparison of density maps (blue mesh) determined from nanodisc- and amphipol-stabilized TRPV1 at various regions of the channel facing the lipid bilayer or at the bilayer surface. Refined atomic models (gold, nanodisc; grey, amphipol) are fit to corresponding densities. Side chain densities were significantly improved in nanodisc-stabilized TRPV1-

DkTx/RTX structure (**a**, **b**), and notable improvement was also seen for unliganded (**c**, **d**) and capsazepine-bound (**e**, **f**) channels in nanodisc.
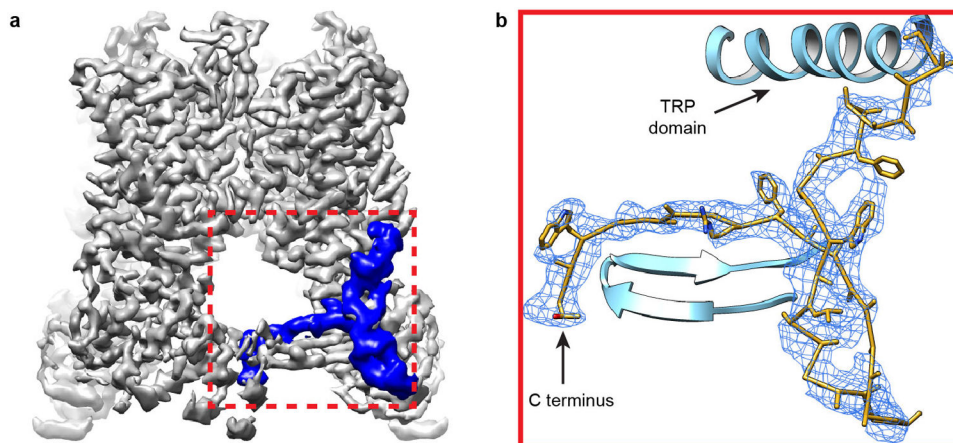

Extended Data Figure 6. Newly resolved TRPV1 cytoplasmic region in nanodisc-stabilized structure

a, A region in TRPV1 C-terminus, previously unresolved in amphipol-stabilized structures (blue) is clearly resolved in the nanodisc-stabilized structure. **b**, Enlarged view of boxed region in (**a**) showing density map (blue mesh) and superimposed model (gold). Previously resolved TRP domain and N-terminal β-strands are depicted in ribbon diagram format (cyan).
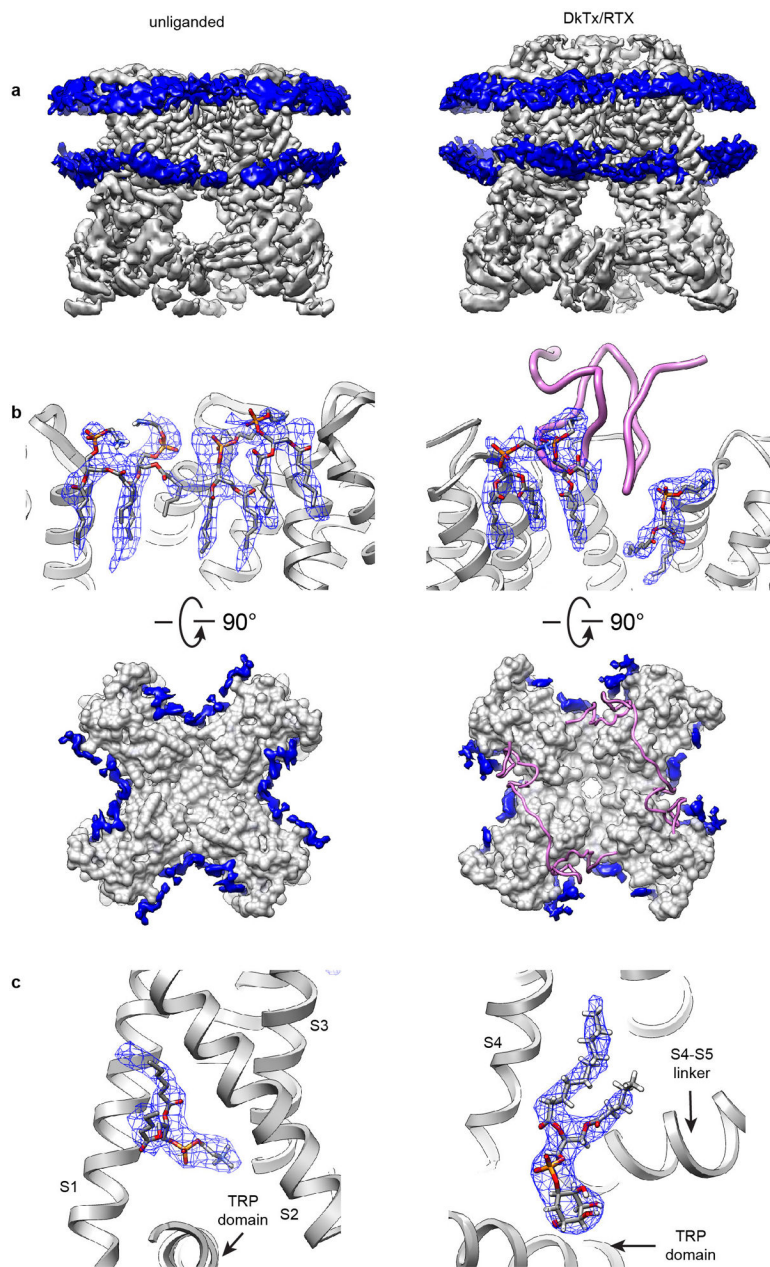
Extended Data Figure 7. Categories of lipid densities observed in TRPV1 structures
a, Two continuous layers of density (blue) contributed by lipid head groups of bilayer within
nanodisc are shown for apo channel (left) and channel in complex with RTX/DkTx (right).
b, Atomic model of annular lipids could be built into well resolved densities (blue mesh)
surrounding the channel protein. DkTx is shown as ribbon diagram (pink). Top-down views
show distribution of resolved annular lipids (blue) in inter-subunit crevices at the outer
leaflet of the membrane. **c**, Well-resolved densities (blue mesh) in the structures representing
a phosphatidylcholine molecule (left) and a phosphatidylinositol molecule (right).
Transmembrane helices of TRPV1 close to the binding site are also shown as ribbon
diagrams (grey).
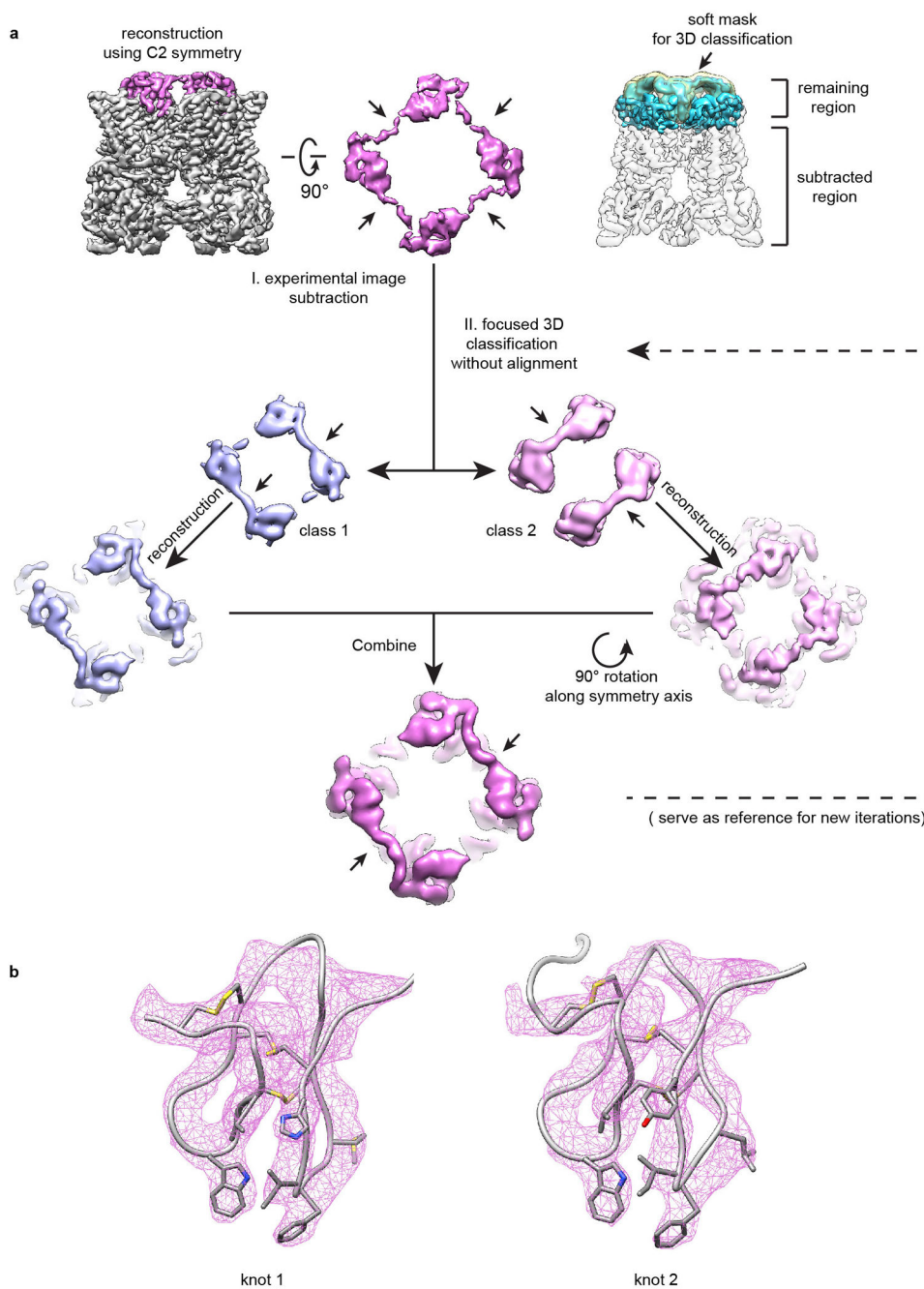
Extended Data Figure 8. Focused analysis of DkTx density map
a, Flow-chart showing procedures of focused 3D classification of DkTx and proximal regions (see Methods section for details). **b**, Atomic models for both knots of DkTx are superimposed on density maps (pink mesh).
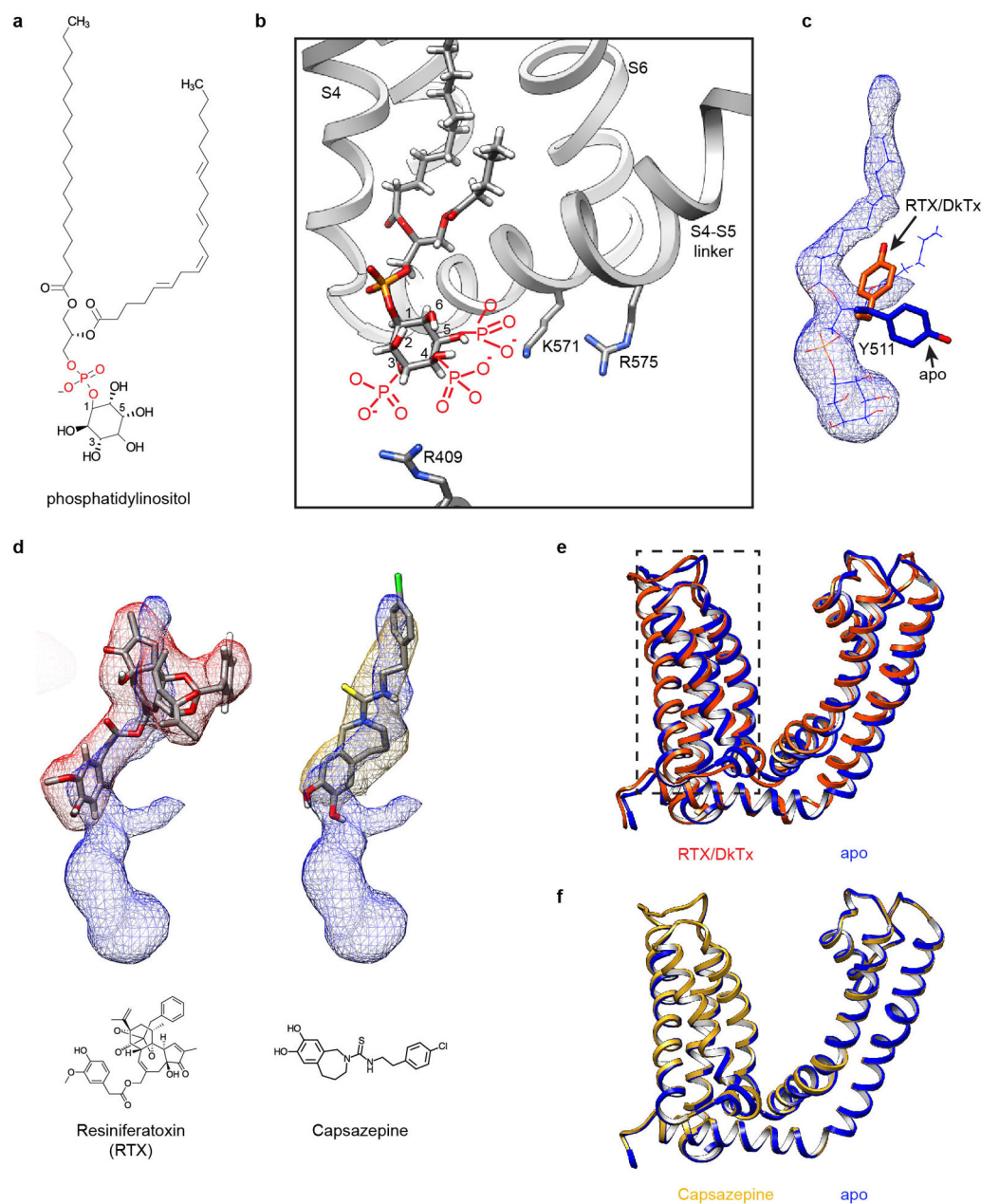
Extended Data Figure 9. Lipid co-factor and vanilloids at the vanilloid binding site of TRPV1
a, Chemical structure of phosphatidylinositol. **b**, Local environment of the phosphatidylinositol binding site may accommodate multiple phosphatidylinositide species with phosphate substituents at 3, 4 and/or 5 positions of the inositol ring (drawn in red). Adjacent regions of the channel are shown as ribbon diagram (grey). **c**, Tyr511 assumes two possible orientations that differ in apo versus agonist-bound states of the TRPV1 channel. In the apo state, one acyl chain of the resident phosphatidylinositol lipid (blue mesh superimposed with atomic model) prevents the Tyr511 side chain from assuming the upward rotamer position. **d**, Density maps of vanilloids (resiniferatoxin, red mesh; capsazepine, gold mesh) superimposed with density of the bound phosphatidylinositol lipid (blue mesh),

suggesting that they occupy overlapping, but not identical sites. Atomic models for both drugs and their chemical structures are also shown. **e**, Overlap of transmembrane region of one TRPV1 subunit corresponding to apo (blue) and RTX/DkTx-bound (orange) states. Note the relatively small conformational change of the voltage sensor-like domain (S1–S4, boxed region). **f**, Overlap of transmembrane region of one TRPV1 subunit corresponding to apo (blue) and capsazepine-bound (gold) states.

Extended Data Table 1

Comparison of imaging/data-processing variables between nanodisc and amphipol datasets

	unliganded	DkTx/RTX	capsazepine
Data collection/processing			
Voltage (kV)	300	300	300
Magnification	31000	31000	31000
Defocus range (μn)	−0.7 – −2.2	−0.7 – −2.2	−0.7 – −2.2
Pixel size (Å)	1.2156	1.2156	1.2156
Total electron dose (e−/Å^2)	41	41	41
Exposure time (s)	6	6	6
Number of images	1000	1200	1219
Number of frames per image	30	30	30
Initial particle number	159193	218787	198831
Final particle number	30689	73929	80725
Resolution (unmasked, Å)	3.53	3.24	3.88
Resolution (masked, Å)	3.28	2.95	3.43
Refinement			
Number of atoms	13360	13722	11928
Protein	11804	12570	11744
Ligand	1556	1152	184
R.m.s deviations			
Bond lengths (Å)	0.011	0.011	0.024
Bond angles (°)	0.911	1.246	1.502
Ramachandran			
Favored (%)	90.3	86.9	86.9
Allowed (%)	9.2	12.9	11.8
Outlier (%)	0.5	0.2	1.3
Molprobity score	2.13	2.25	2.55

	Unliganded		DkTx/RTX		Capsazepiine	
	nanodisc	amphipol	nanodisc	amphipol	nanodisc	amphipol
Defocus range (μn)	−0.7– −2.2	−1.5– −3.0	−0.7– −2.2	−1.5– −3.0	−0.7 – −2.2	−0.8 – −2.2
Number of images	1000	946	1200	−1000	1219	1002
Motion correction	UcsfDfCorr	MotionCorr	UcsfDfCorr	MotionCorr	UcsfDfCorr	MotionCorr
Initial particle #	159193	97166	218787	148670	198831	81709

|	Unliganded		DkTx/RTX		Capsazepiine	
	nanodisc	amphipol	nanodisc	amphipol	nanodisc	amphipol
Final particle #	30689	35645	73929	36158	80725	47477
Resolution (Å)	3.28	3.28	2.95	3.8	3.43	3.8

Acknowledgments

References

1. Hilgemann DW. Getting ready for the decade of the lipids. Annu Rev Physiol. 2003; 65:697–700. [PubMed: 12517999]

2. Hille B, Dickson EJ, Kruse M, Vivas O, Suh BC. Phosphoinositides regulate ion channels. Biochim Biophys Acta. 2015; 1851:844–856. [PubMed: 25241941]

3. Lee AG. Biological membranes: the importance of molecular detail. Trends Biochem Sci. 2011; 36:493–500. [PubMed: 21855348]

4. Caffrey M. A lipid's eye view of membrane protein crystallization in mesophases. Curr Opin Struct Biol. 2000; 10:486–497. [PubMed: 10981640]

5. Landau EM, Rosenbusch JP. Lipidic cubic phases: a novel concept for the crystallization of membrane proteins. Proc Natl Acad Sci U S A. 1996; 93:14532–14535. [PubMed: 8962086]

6. Gonen T, et al. Lipid-protein interactions in double-layered two-dimensional AQP0 crystals. Nature. 2005; 438:633–638. [PubMed: 16319884]

7. Wang L, Sigworth FJ. Structure of the BK potassium channel in a lipid membrane from electron cryomicroscopy. Nature. 2009; 461:292–295. [PubMed: 19718020]

8. Bayburt TH, Grinkova YV, Sligar SG. Self-Assembly of Discoidal Phospholipid Bilayer Nanoparticles with Membrane Scaffold Proteins. NanoLetters. 2002; 2:853–856.

9. Banerjee S, Huber T, Sakmar TP. Rapid incorporation of functional rhodopsin into nanoscale apolipoprotein bound bilayer (NABB) particles. Journal of molecular biology. 2008; 377:1067–1081. [PubMed: 18313692]

10. Ritchie TK, et al. Chapter 11 - Reconstitution of membrane proteins in phospholipid bilayer nanodiscs. Methods Enzymol. 2009; 464:211–231. [PubMed: 19903557]

11. Efremov RG, Leitner A, Aebersold R, Raunser S. Architecture and conformational switch mechanism of the ryanodine receptor. Nature. 2015; 517:39–43. [PubMed: 25470059]

12. Frauenfeld J, et al. Cryo-EM structure of the ribosome-SecYE complex in the membrane environment. Nat Struct Mol Biol. 2011; 18:614–621. [PubMed: 21499241]

13. Bai XC, McMullan G, Scheres SH. How cryo-EM is revolutionizing structural biology. Trends Biochem Sci. 2015; 40:49–57. [PubMed: 25544475]

14. Cheng Y. Single-Particle Cryo-EM at Crystallographic Resolution. Cell. 2015; 161:450–457. [PubMed: 25910205]

15. Kuhlbrandt W. Cryo-EM enters a new era. Elife. 2014; 3:e03678. [PubMed: 25122623]

16. Bevan S, Quallo T, Andersson DA. Trpv1. Handb Exp Pharmacol. 2014; 222:207–245. [PubMed: 24756708]

17. Julius D. TRP channels and pain. Annu Rev Cell Dev Biol. 2013; 29:355–384. [PubMed: 24099085]

18. Cao E, Liao M, Cheng Y, Julius D. TRPV1 structures in distinct conformations reveal activation mechanisms. Nature. 2013; 504:113–118. [PubMed: 24305161]

19. Liao M, Cao E, Julius D, Cheng Y. Structure of the TRPV1 ion channel determined by electron cryo-microscopy. Nature. 2013; 504:107–112. [PubMed: 24305160]

20. Long SB, Tao X, Campbell EB, MacKinnon R. Atomic structure of a voltage-dependent K+ channel in a lipid membrane-like environment. Nature. 2007; 450:376–382. [PubMed: 18004376]

21. Szallasi A, Blumberg PM. Resiniferatoxin, a phorbol-related diterpene, acts as an ultrapotent analog of capsaicin, the irritant constituent in red pepper. Neuroscience. 1989; 30:515–520. [PubMed: 2747924]

22. Bohlen CJ, et al. A bivalent tarantula toxin activates the capsaicin receptor, TRPV1, by targeting the outer pore domain. Cell. 2010; 141:834–845. [PubMed: 20510930]

23. Chou MZ, Mtui T, Gao YD, Kohler M, Middleton RE. Resiniferatoxin binds to the capsaicin receptor (TRPV1) near the extracellular side of the S4 transmembrane domain. Biochemistry. 2004; 43:2501–2511. [PubMed: 14992587]

24. Gavva NR, et al. Molecular determinants of vanilloid sensitivity in TRPV1. J Biol Chem. 2004; 279:20283–20295. [PubMed: 14996838]

25. Hanson SM, Newstead S, Swartz KJ, Sansom MSP. Capsaicin Interaction with TRPV1 Channels in a Lipid Bilayer: Molecular Dynamics Simulation. Biophysical journal. 2015; 108:1425–1434. [PubMed: 25809255]

26. Jordt SE, Julius D. Molecular basis for species-specific sensitivity to "hot" chili peppers. Cell. 2002; 108:421–430. [PubMed: 11853675]

27. Phillips E, Reeve A, Bevan S, McIntyre P. Identification of species-specific determinants of the action of the antagonist capsazepine and the agonist PPAHV on TRPV1. J Biol Chem. 2004; 279:17165–17172. [PubMed: 14960593]

28. Yang F, et al. Structural mechanism underlying capsaicin binding and activation of the TRPV1 ion channel. Nat Chem Biol. 2015; 11:518–524. [PubMed: 26053297]

29. Bevan S, et al. Capsazepine: a competitive antagonist of the sensory neurone excitant capsaicin. Br J Pharmacol. 1992; 107:544–552. [PubMed: 1422598]

30. Boukalova S, Marsakova L, Teisinger J, Vlachova V. Conserved residues within the putative S4–S5 region serve distinct functions among thermosensitive vanilloid transient receptor potential (TRPV) channels. Journal of Biological Chemistry. 2010; 285:41455–41462. [PubMed: 21044960]

31. Lee SY, MacKinnon R. A membrane-access mechanism of ion channel inhibition by voltage sensor toxins from spider venom. Nature. 2004; 430:232–235. [PubMed: 15241419]

32. Milescu M, et al. Interactions between lipids and voltage sensor paddles detected with tarantula toxins. Nat Struct Mol Biol. 2009; 16:1080–1085. [PubMed: 19783984]

33. Milescu M, et al. Tarantula toxins interact with voltage sensors within lipid membranes. J Gen Physiol. 2007; 130:497–511. [PubMed: 17938232]

34. Bae C, et al. Structural insights into the mechanism of activation of the TRPV1 channel by a membrane-bound tarantula toxin. Elife. 2016; 5

35. Hardie RC. TRP channels and lipids: from Drosophila to mammalian physiology. J Physiol. 2007; 578:9–24. [PubMed: 16990401]

36. Qin F. Regulation of TRP ion channels by phosphatidylinositol-4,5-bisphosphate. Handb Exp Pharmacol. 2007:509–525. [PubMed: 17217076]

37. Rohacs T. Phosphoinositide regulation of TRPV1 revisited. Pflugers Arch. 2015; 467:1851–1869. [PubMed: 25754030]

38. Cao E, Cordero-Morales JF, Liu B, Qin F, Julius D. TRPV1 channels are intrinsically heat sensitive and negatively regulated by phosphoinositide lipids. Neuron. 2013; 77:667–679. [PubMed: 23439120]

39. Prescott ED, Julius D. A modular PIP2 binding site as a determinant of capsaicin receptor sensitivity. Science. 2003; 300:1284–1288. [PubMed: 12764195]

40. Ufret-Vincenty CA, et al. Mechanism for phosphoinositide selectivity and activation of TRPV1 ion channels. J Gen Physiol. 2015; 145:431–442. [PubMed: 25918361]

41. Ufret-Vincenty CA, Klein RM, Hua L, Angueyra J, Gordon SE. Localization of the PIP2 sensor of TRPV1 ion channels. J Biol Chem. 2011; 286:9688–9698. [PubMed: 21224382]

42. Hansen SB, Tao X, MacKinnon R. Structural basis of PIP2 activation of the classical inward rectifier K+ channel Kir2.2. Nature. 2011; 477:495–498. [PubMed: 21874019]

43. Booth DS, Avila-Sakar A, Cheng Y. Visualizing proteins and macromolecular complexes by negative stain EM: from grid preparation to image acquisition. J Vis Exp. 2011

44. Li X, et al. Electron counting and beam-induced motion correction enable near-atomic-resolution single-particle cryo-EM. Nat Methods. 2013; 10:584–590. [PubMed: 23644547]

45. Li X, Zheng S, Agard DA, Cheng Y. Asynchronous data acquisition and on-the-fly analysis of dose fractionated cryoEM images by UCSFImage. J Struct Biol. 2015; 192:174–178. [PubMed: 26370395]

46. Rohou A, Grigorieff N. CTFFIND4: Fast and accurate defocus estimation from electron micrographs. J Struct Biol. 2015; 192:216–221. [PubMed: 26278980]

47. Frank J, et al. SPIDER and WEB: processing and visualization of images in 3D electron microscopy and related fields. Journal of structural biology. 1996; 116:190–199. [PubMed: 8742743]

48. Grant T, Grigorieff N. Measuring the optimal exposure for single particle cryo-EM using a 2.6 A reconstruction of rotavirus VP6. Elife. 2015; 4:e06980. [PubMed: 26023829]

49. Scheres SHW. RELION: implementation of a Bayesian approach to cryo-EM structure determination. Journal of structural biology. 2012; 180:519–530. [PubMed: 23000701]

50. Scheres SHW, Chen S. Prevention of overfitting in cryo-EM structure determination. Nature methods. 2012; 9:853–854. [PubMed: 22842542]

51. Kucukelbir A, Sigworth FJ, Tagare HD. Quantifying the local resolution of cryo-EM density maps. Nature methods. 2014; 11:63–65. [PubMed: 24213166]

52. Hohn M, et al. SPARX, a new environment for Cryo-EM image processing. J Struct Biol. 2007; 157:47–55. [PubMed: 16931051]

53. Tang G, et al. EMAN2: an extensible image processing suite for electron microscopy. Journal of structural biology. 2007; 157:38–46. [PubMed: 16859925]

54. Pettersen EF, et al. UCSF Chimera--a visualization system for exploratory research and analysis. J Comput Chem. 2004; 25:1605–1612. [PubMed: 15264254]

55. Emsley P, Lohkamp B, Scott WG, Cowtan K. Features and development of Coot. Acta Crystallographica Section D: Biological Crystallography. 2010; 66:486–501. [PubMed: 20383002]

56. Moriarty NW, Grosse-Kunstleve RW, Adams PD. electronic Ligand Builder and Optimization Workbench (eLBOW): a tool for ligand coordinate and restraint generation. Acta Crystallographica Section D: Biological Crystallography. 2009; 65:1074–1080. [PubMed: 19770504]

57. Adams PD, et al. PHENIX: a comprehensive Python-based system for macromolecular structure solution. Acta Crystallographica Section D: Biological Crystallography. 2010; 66:213–221. [PubMed: 20124702]

58. van Aalten DMF, et al. PRODRG, a program for generating molecular topologies and unique molecular descriptors from coordinates of small molecules. Journal of computer-aided molecular design. 1996; 10:255–262. [PubMed: 8808741]

59. Afonine PV, Headd JJ, Terwilliger TC, Adams PD. New tool: phenix. real_space_refine. Computational Crystallography Newsletter. 2013; 4:43–44.

60. Amunts A, et al. Structure of the yeast mitochondrial large ribosomal subunit. Science. 2014; 343:1485–1489. [PubMed: 24675956]

61. Chen VB, et al. MolProbity: all-atom structure validation for macromolecular crystallography. Acta Crystallographica Section D: Biological Crystallography. 2009; 66:12–21. [PubMed: 20057044]
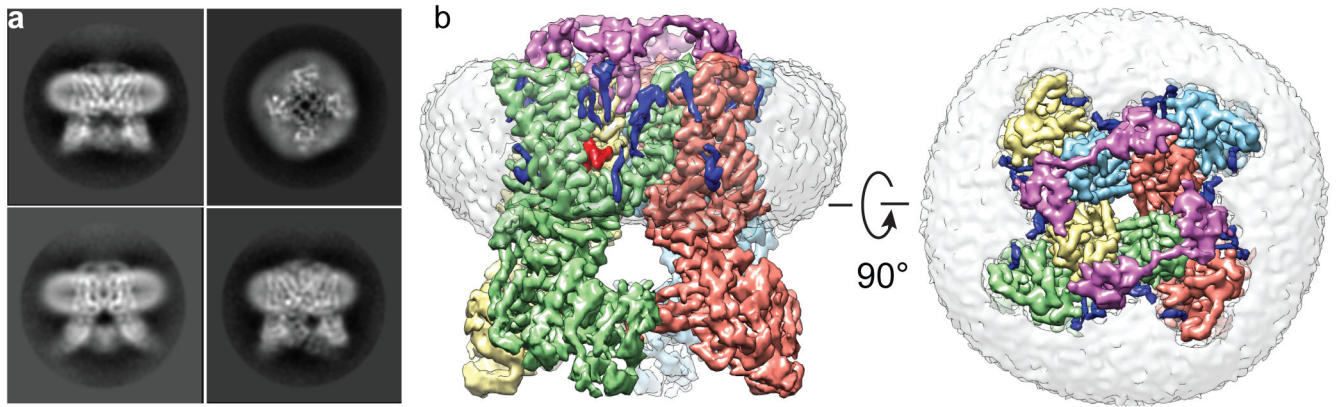
Figure 1. TRPV1 structures determined in lipid nanodisc
a, Side and top views of reference-free 2D class averages of TRPV1 in nanodiscs, showing transmembrane helices and lipid bilayer. **b**, Side and top views of 3D reconstruction of TRPV1-ligand-nanodisc complex. Individual channel subunits are color-coded with two molecules of DkTx (purple) atop the channel and a molecule of RTX (red) in the vanilloid binding pocket. Densities of the nanodisc (grey) and well-resolved lipids (blue) are also shown.
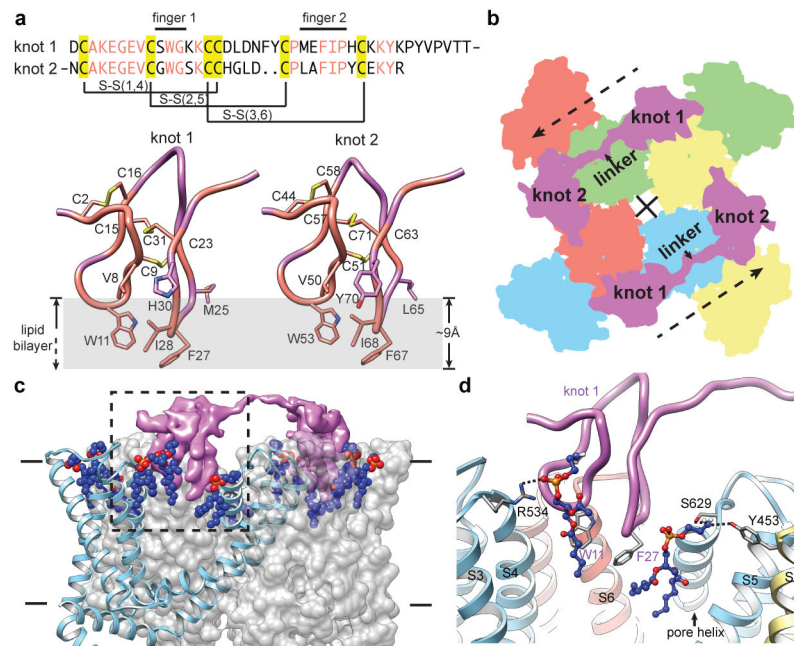
Figure 2. Structural details of tripartite toxin-channel-lipid complex
a, Sequence of DkTx (top) showing location of intramolecular disulfide bonds and finger-like loops formed primarily by residues conserved between toxin knots (orange). Hydrophobic residues enable fingers to penetrate the lipid bilayer by ~9Å (bottom). **b**, Schematic top down view showing antiparallel arrangement of two DkTx molecules (purple) binding at subunit interfaces of a TRPV1 homo-tetramer (subunits are color-coded). **c**, Cutaway view depicting one DkTx molecule interacting with two adjacent TRPV1 subunits (grey) and associated lipids (blue spheres; red and orange spheres depict phosphate head groups). Superimposed ribbon diagram (light blue) denotes location of transmembrane α-helices for one channel subunit. **d**, Detailed view of boxed region in (**c**) showing interactions between lipids and amino acid side chains from channel and toxin (dotted line, hydrogen bond). Helices from three neighboring channel subunits are color-coded as in (**b**).
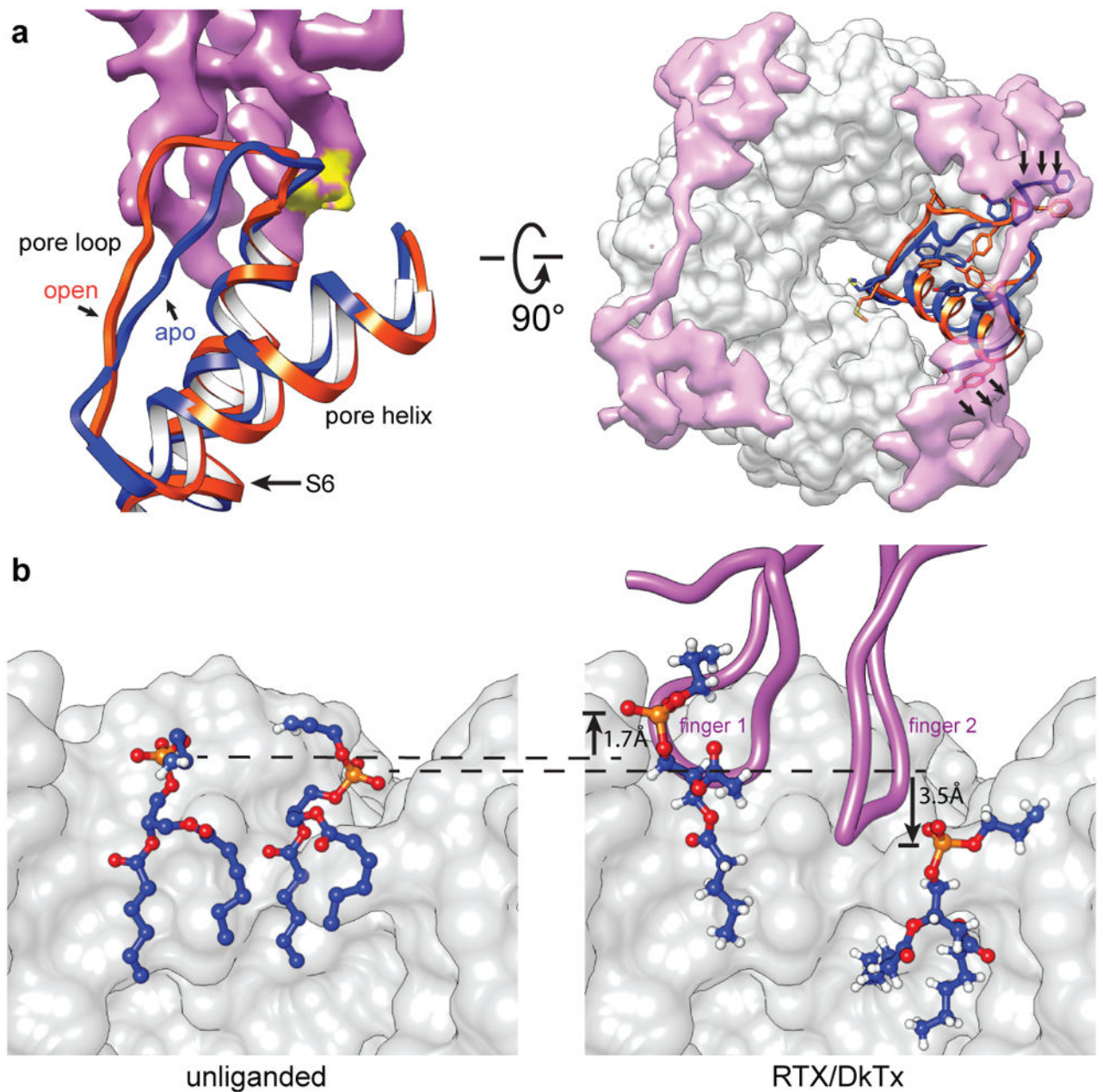
Figure 3. Movement of protein and lipids associated with toxin binding
a, Movement of pore loop, pore helix, and part of S6 domain from closed (blue) to open (orange) states upon DkTx (purple) binding. Without such movement, one finger of DkTx would clash (yellow region) with the unliganded channel at the top of S6. Top down view (right) shows two DkTx molecules atop TRPV1 (grey density). Toxin binding is associated with lateral shifts of the pore helix and loop (arrows), as well as large rearrangements of aromatic side chains within these regions. **b**, Two annular lipids (shown in blue, with phosphate in orange and oxygen in red) at the channel-toxin interface undergo both lateral and vertical movements upon DkTx binding. Dashed lines mark original position of
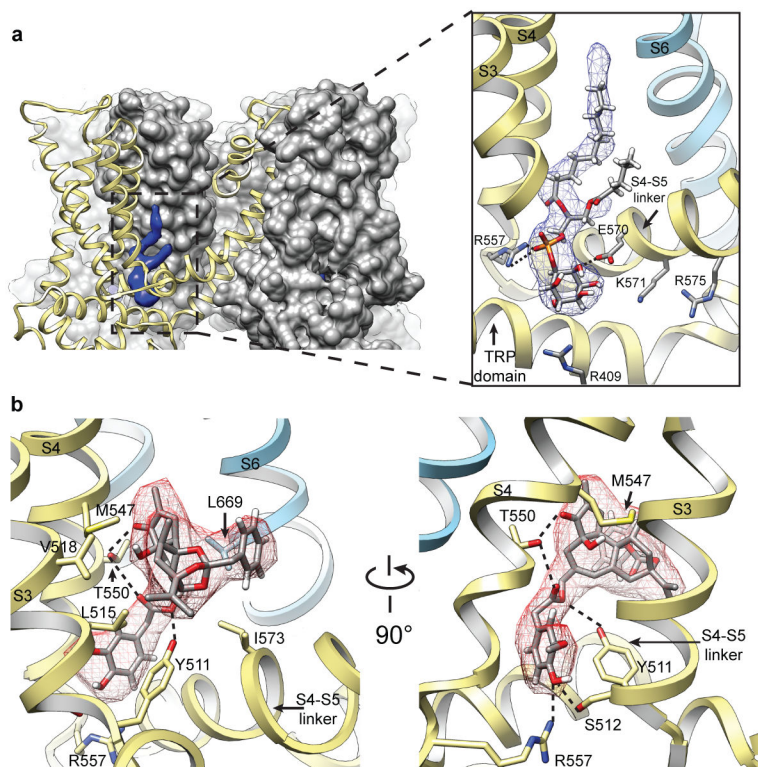
phosphate groups in the absence of toxin (left); arrows indicate displacement of lipids in the presence of toxin (right).

**Figure 4. Shared binding pocket for phosphatidylinositol lipids and vanilloid ligands**

a, Surface representation of TRPV1 (grey) in cutaway view revealing location of bound co-factor (blue). Superimposed ribbon diagram (yellow) denotes location of transmembrane α-helices for one channel subunit. Detailed view of boxed region shows how co-factor density (blue mesh) accommodates a molecule of phosphatidylinositol (PI). Positive and negative side chains from S4 and S4–S5 linker, respectively, can form ionic interactions with negatively charged phosphate or hydroxyl moieties on inositol ring. Helices from a neighboring subunit (light blue) are also shown. **b**, Density for resiniferatoxin (RTX, red mesh) is well fit by its atomic structure. Residues essential for RTX sensitivity (Y511, M547, T550) lie in close proximity to the ligand and can engage in electrostatic or hydrophobic interactions. Densities for PI and RTX define overlapping, but non-identical sites (also see Extended Data Fig. 9).
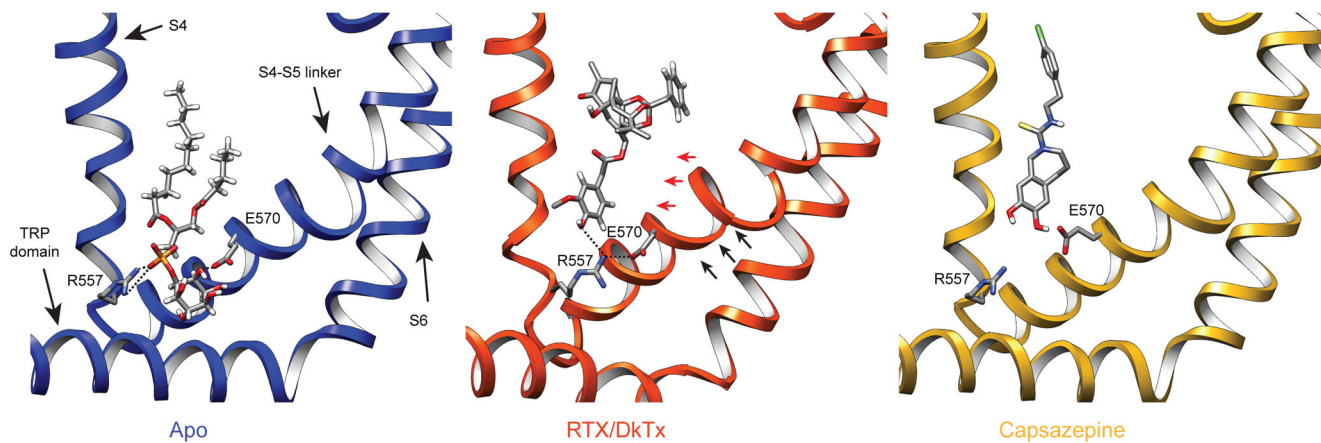
Figure 5. Structural rearrangements associated with vanilloid binding

a, Ribbon diagrams depicting relative locations of S4, S4–S5 linker, S6 and TRP domain helices in the presence of phosphatidylinositol (blue, left), resiniferatoxin (orange, middle), or capsazepine (gold, right). Vanillyl ring of RTX uniquely stabilizes interaction between Arg557 and Glu570 to facilitate movement of the S4–S5 linker away from the central axis of the channel (indicated by red arrows), thereby facilitating opening of the lower gate through coupled movements (indicated by black arrows).
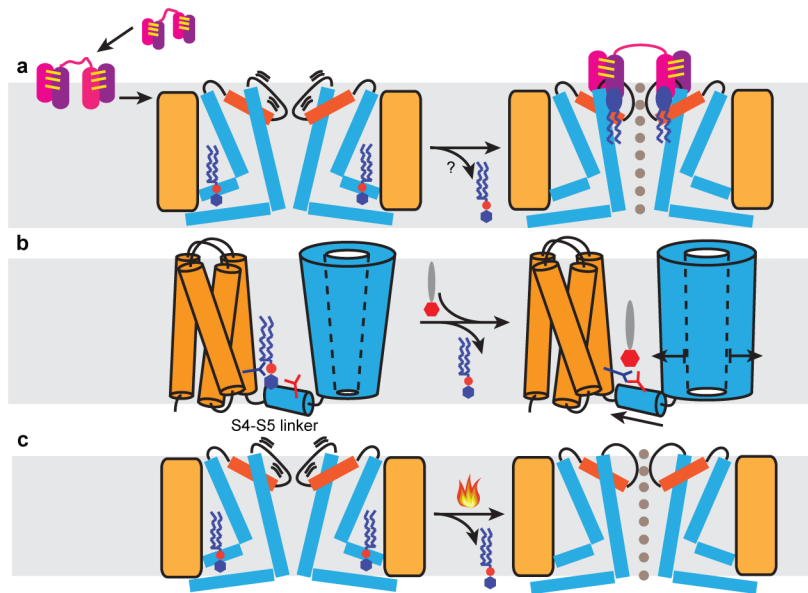
Figure 6. Mechanistic models for TRPV1 activation
a, Proposed mechanism for DkTx action. Two hydrophobic fingers (purple and pink) of each ICK knot (joined by three intramolecular disulfide bonds, yellow lines) enable the toxin to partition into the lipid bilayer (grey shade) and subsequently target TRPV1. In the closed state, the upper pore region of the channel (orange, pore helix; thick line, pore loop) undergoes brief spontaneous excursions to an open state, enabling DkTx to dock. Several annular lipids (blue ellipse with zigzag tails) bind at the channel-toxin interface to further stabilize the open state through formation of a tripartite complex. Resident phosphatidylinositides (blue hexagon attached to red sphere with zigzag tails) in the vanilloid pocket may leave upon toxin binding to facilitate allosteric opening of the lower gate. **b**, Proposed mechanism for vanilloid agonist action. Phosphatidylinositide co-factor binds in vanilloid pocket to stabilize the channel in its closed state. Vanilloid agonist (red hexagon attached to grey ellipse) displaces phosphatidylinositide to facilitate formation of a salt bridge between Arg557 (dark blue branch) and Glu570 (red branch), consequently pulling the S4–S5 linker away from the channel's central axis to open the lower gate. **c**, Heat may open the channel through a similar mechanism involving thermal displacement of resident phosphatidylinositides.